Article

Enhanced Performance of Fluidic Phononic Crystal Sensors Using Different Quasi-Periodic Crystals

Ahmed G. Sayed [1], Ali Hajjiah [2], Mehdi Tlija [3], Stefano Bellucci [4,*], Mostafa R. Abukhadra [5], Hussein A. Elsayed [1] and Ahmed Mehaney [1,*]

[1] Physics Department, Faculty of Science, Beni-Suef University, Beni Suef 62512, Egypt; drhussien85sc@gmail.com
[2] Department of Electrical Engineering, College of Engineering and Petroleum, Kuwait University, Safat 13113, Kuwait
[3] Industrial Engineering Department, College of Engineering, King Saud University, P.O. Box 800, Riyadh 11421, Saudi Arabia
[4] INFN-Laboratori Nazionali di Frascati, Vie. E. Fermi 54, 00044 Frascati, Italy
[5] Materials Technologies and Their Applications Lab, Faculty of Science, Beni-Suef University, Beni Suef 62511, Egypt
* Correspondence: bellucci@inf.infn.it (S.B.); ahmed011236@science.bsu.edu.eg (A.M.)

Abstract: In this paper, we introduce a comprehensive theoretical study to obtain an optimal highly sensitive fluidic sensor based on the one-dimensional phononic crystal (PnC). The mainstay of this study strongly depends on the high impedance mismatching due to the irregularity of the considered quasi-periodic structure, which in turn can provide better performance compared to the periodic PnC designs. In this regard, we performed the detection and monitoring of the different concentrations of lead nitrate ($Pb(NO_3)_2$) and identified it as being a dangerous aqueous solution. Here, a defect layer was introduced through the designed structure to be filled with the $Pb(NO_3)_2$ solution. Therefore, a resonant mode was formed within the transmittance spectrum of the considered structure, which in turn shifted due to the changes in the concentration of the detected analyte. The numerical findings demonstrate the role of the different sequences such as Fibonacci, Octonacci, Thue–Morse, and double period on the performance of the designed PhC detector. Meanwhile, the findings of this study show that the double-period quasi-periodic sequence provides the best performance with a sensitivity of 502.6 Hz/ppm, a damping rate of 5.9×10^{-5}, a maximum quality factor of 8463.5, and a detection limit of 2.45.

Keywords: quasi-periodic; phononic crystals; acoustic waves; sensors; heavy metal; resonance

1. Introduction

Artificial periodic structures, which demonstrate sound wave propagation, are referred to as phononic crystals (PnCs). The phononic band gap (PnBG) is considered one of the PnCs' most remarkable features due to its ability to confine the propagation of sound waves through the PnC structures [1,2]. The sustainability of these gaps is frequently investigated by the mechanical properties of PnCs' constituent materials [2]. It is worth noting that PhCs have recently received significant attention due to their ability to control not only the sound waves but also a broad band of mechanical waves ranging from audible frequency range (i.e., 1–20 kHz) to THz frequencies [1–3]. Therefore, PnCs have a significant role in a variety of engineering applications such as temperature sensors, seismic wave reflection, liquid sensors, heat isolation systems, waveguides, acoustic cloaking, multiplexing systems, filters, actuators, and acoustic metamaterials' fabrication [4–6]. More specifically, acoustic sensors, which incorporate PnCs, provide some innovative designs for detecting and differentiating between the different chemical and biological components [4,7,8]. In this regard, Aly et al. proposed a one-dimensional (1D) PnC structure for sensing and detection applications [9].

Another PnC sensor was proposed by Zubtsov et al. to gauge a water/1-propanol solution's concentration [10]. Two weakly coupled point defects in a liquid–solid phononic crystal were used for sensing liquid concentrations, and a specific example of methanol in ethanol was examined [11]. Also, the detection of toxic gases based on some PnC designs has also received considerable attention. For example, Shrouk et al. theoretically proposed a defected PnC as a specific gas sensor, which was used to detect several toxic gases, including CH_4, O_2, CO_2, and NH_3 [12]. Furthermore, Hadiseh et al. demonstrated the role of some periodic and quasi-periodic PnC designs as gas sensors for monitoring NH_3, CH_4, O_2, and CO_2 [13]. In addition, Mohamed A. Basyooni et al. conducted an experimental study for monitoring CO_2 concentrations based on nanostructured thin films [14].

Recently, many researchers have directed considerable attention toward the detection of heavy metal concentrations in freshwater [15]. Notably, the density of heavy metals is five times higher compared to freshwater. Unfortunately, these elements exhibit various detrimental impacts on human health due to the toxicity that is associated with their bulk density [16–18]. Thus, environmental concerns, as well as health concerns, have lately increased due to hazardous environmental issues because of heavy metal contamination [19–21]. The Earth's crust contains trace amounts of these naturally occurring metals. Anthropogenic activities like mining, farming, smelting, and industrial processes are often the source of human exposure [22–25]. After being discharged into the environment, heavy metals can enter the human body through inhaling and ingestion. These metals may accumulate in human tissues more quickly than the body can detoxicate them.

Lead and nitrite ions are combined to produce a dangerous chemical substance, which is referred to as $Pb(NO_3)_2$ [26]. It can seriously jeopardize both human and animal health. $Pb(NO_3)_2$ exposure may occur through skin contact, inhalation, or ingestion. Lead as a dangerous heavy metal may accumulate throughout the body, leading to terrible impacts on the nervous system, immune system, hematopoiesis, digestive system, kidneys, reproduction, development, and cardiovascular. Also, carcinogenic compounds can be produced via the reaction of nitrites with other molecules [20]. $Pb(NO_3)_2$ can also cause learning impairments, behavioral issues, and reduced cognitive function, and it is extremely harmful to the nervous system, especially in youngsters. Anemia, gastrointestinal diseases, renal damage, and reproductive and cardiovascular problems could be due to $Pb(NO_3)_2$ exposure. To prevent lead nitrite poisoning, lead and its compounds must be strictly managed to prevent environmental effects [27,28].

In the context of heavy metal detection, it is crucial to accurately and efficiently identify such substances to prevent their harmful effects. Currently, many existing methods for detecting heavy metals rely on nanoparticles and intricate designs. Recently, PnC structures have been introduced to detect the concentrations of heavy metals. For example, PnCs have been introduced as a demultiplexer for detecting $CuSO_4$, $MgSO_4$, and $MnSO_4$ hazardous heavy metals in water with concentrations more than 1% [10,29].

Notably, quasi-periodic structures lack translational symmetry and represent a specific design that falls between periodic and aperiodic structures [30,31]. It displays a certain form of spatial ordering. Different rules, like the Octonacci, double-period, Fibonacci, Thue–Morse sequences, etc., can be used to create quasi-periodic structures [32,33].

Because these structures provide omnidirectional band gaps and large photonic and phononic band gaps, they are more effective compared to the periodic designs. Since it is easy to fabricate waveguides and cavities in photonic crystals, they are regarded as the most optimum choice for tuning transmission modes [34]. Even when they are constructed with smaller sizes, quasi-periodic structures offer a viable option to overcome the difficulty of creating low-frequency PnBGs compared to periodic or defective structures [35].

Notably, 1D Fibonacci quasi-crystals are a popular type of quasi-crystal that offer an extra degree of customization for photonic and phononic band gaps. The 1D Fibonacci quasi-crystals are capable of producing some omnidirectional photonic band gaps. Moreover, the double-period sequence provides the best performance in detection compared to its counterparts. In addition, quasi-periodic meta crystals are also promising for waveguide

and cavity creation because of their isotropy and presumed defect insensitivity. Hybrid structures, in which periodic and aperiodic structures are blended, are useful for fine-tuning resonance transmission modes [36,37].

Therefore, this study introduces a straightforward and effective design for monitoring and detecting $Pb(NO_3)_2$. This research explores various quasi-periodic sequences to develop an ultrasensitive PnC sensor tailored for measuring heavy metals like $Pb(NO_3)_2$ in low concentrations (i.e., at the ppm scale). The study examines the impact of concentration on sensor performance and delves into optimizing the ideal quasi-crystal type.

In particular, the irregularities within quasi-periodic structures, stemming from variations in geometry, material composition, or boundary conditions, can lead to a pronounced impact on the impedance mismatch compared to the periodic arrangements. The primary objective of this research is to analyze the slight changes in liquid concentrations, particularly focusing on damped forced responses and spectral assessments. By exploring various sequences such as Fibonacci, Octonacci, Thue–Morse, and double period, acoustic transmission spectra were graphed to identify the presence of hazardous $Pb(NO_3)_2$ solutions. Through the utilization of the transfer matrix method (TMM) and MATLAB software, the transmission spectra and numerous performance metrics were computed. The findings indicate that the double-period quasi-periodic sequence exhibits the highest sensitivity among the designs.

2. Theoretical Analysis and Design
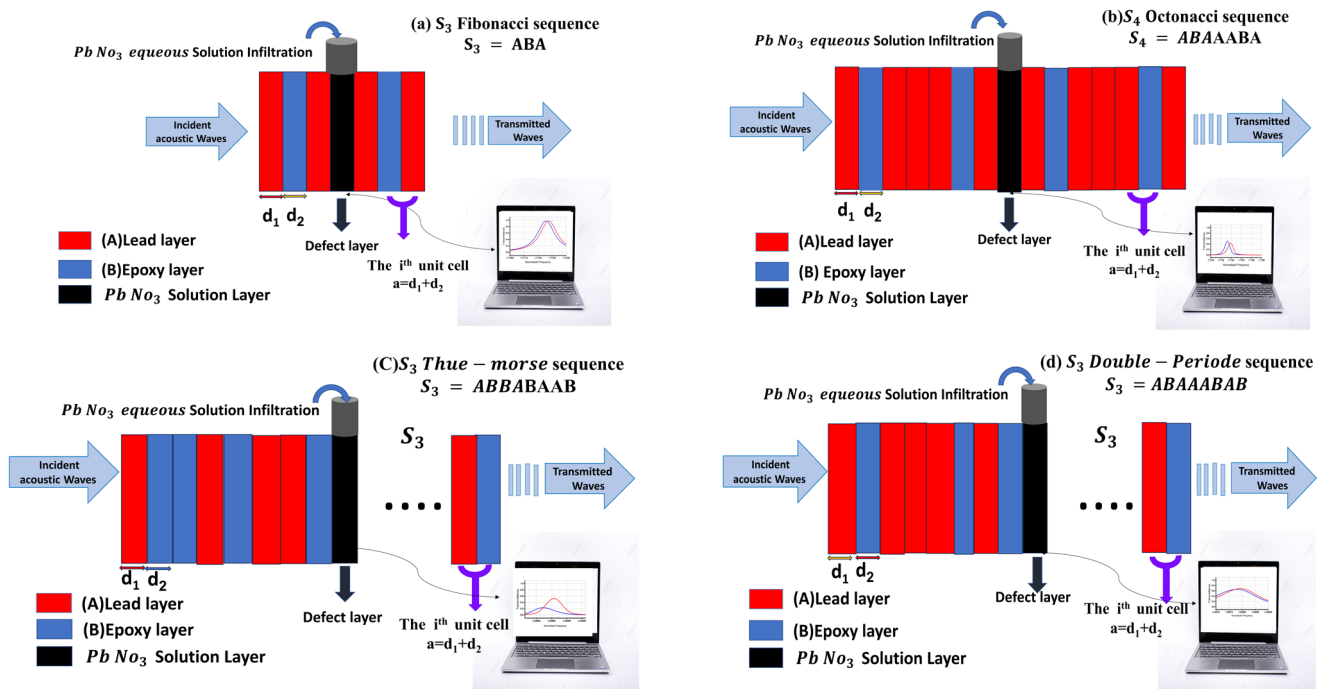
2.1. Designing the Model

In this subsection, we introduce the designs of two different PnC structures based on periodic and quasi-periodic arrangements to detect the low concentrations of $Pb(NO_3)_2$ heavy metals in water. PnBG and slow modes were utilized to establish the detection protocols. The acoustic characteristics of the building materials are illustrated in Table 1. The quasi-periodic design of the 1D PnCs was performed using several sequences like Fibonacci, Octonacci, Thue–Morse, and double period; nevertheless, the periodic crystal's design reflects a regular change in the constructing layers' sound speed and density. In simple terms, periodic designs have a predictable and clear repetition, while quasi-periodic designs feature a more complex and less predictable pattern of repetition. This design is composed of multilayers, which are designed from epoxy mixed with lead (as seen in Figure 1a). The analysis section presents an extensive overview of the stacking rules, which were implemented to generate the quasi-periodic PnC structure. Through the utilization of the different types of quasi-periodic PnC structures, this study investigates the propagation of acoustic waves across these sequences to reach the optimal one to act as a heavy metal sensor. The first formalization of our model design is based on the following factors:

1. The physical properties of lead and epoxy are different. This high acoustic mismatch enhances the formation of a wide band gap, which in turn makes the location of resonant modes easier to achieve.
2. The thickness of each unit cell is given by $a = d_1 + d_2$, where d_1 is the thickness of the first layer, and d_2 is the thickness of the second layer.
3. A transducer to transmit the incident wave is shown on the left-side design in Figure 1, and a detector is shown on the right side to record the acoustic signal.
4. The phononic crystal sensor can detect and measure the transmission spectra of the incident wave by utilizing the crystal's distinctive properties (such as the acoustic properties listed in Table 1) that interact with the incoming wave. The data provided in the first table have been reported in other references [38,39].
5. The phononic crystal sensor was analyzed through various steps, such as detecting the transmission spectra of each proposed quasi-crystal filled with the analyte. This step was performed to demonstrate the optimum design for achieving excellent performance. Secondly, by utilizing band gap effects and analyzing the spectral characteristics of each analyte concentration, the sensor could identify small changes in heavy metal concentrations by examining the spectral components of the transmitted

wave. Lastly, the sensor's performance was adjusted by computing metrics such as sensitivity.

Table 1. Mass density and sound speed of the building materials used in the introduced PnC structure.

Material	Mass Density $\rho \times 10^3$ (kg m^{-3})	Sound Speed c (m s^{-1})	Thickness d (μm)
Lead	11.4	1960.12	0.5
Epoxy	1.18	2539.518	0.1
PbNo$_3$	Concentration-dependent	Concentration-dependent	0.1

Figure 1. The proposed sensor's schematic diagram using several quasi-periodic sequences: (**a**) the Fibonacci sequence; (**b**) the Octonacci sequence; (**c**) the Thue–Morse sequence; (**d**) the double-period sequence.

One of the earlier representations of an aperiodic chain is the Fibonacci sequence [40,41]. An experimental implementation of a Fibonacci structure is accomplished via positioning A and B, i.e., the two building blocks, where the nth order of this sequence (S_n) is given by a recursive formula as follows:

$$S_n = S_{n-1} S_{n-2} \qquad (1)$$

where $n \geq 2$.

In the above formula, S_0 = B and S_1 = A; therefore, the upcoming series is obtained as $S_2 = AB$, $S_3 = ABA$, $S_4 = ABAAB$, etc. Remarkably, it possesses an unchanged characteristic under A → AB and B → A transformations. When a specific defect layer was placed between two layers that possess a similar Fibonacci sequence pattern, an aqueous sensor with a specified defective quasi-periodic PnC structure was produced (see Figure 1a). After that, the proposed liquid sensor was contrasted with the quasi-periodic PnC structure of S_3 [(S_3) ($PbNo_3$ *solution*) (S_3)]. A designated defect layer was thus included in the center of this design, which would be filled with $PbNo_3$. Here, the lattice constant of every unit cell length was obtained by $a = d_1 + d_2$, where the thickness of the lead and epoxy in the first layer and the second layer were 0.5 μm and 0.1 μm, correspondingly.

As shown in Figure 1b, one of the most important quasi-periodic sequences is the Octonacci sequence [42], such that the nth order of this sequence (S_n) is given as follows:

$$S_n = S_{n-1} \, S_{n-2} \, S_{n-1} \tag{2}$$

where $n \geq 3$.

To begin with, S_1 = B and S_2 = A; therefore, S_3 = ABA and S_4 = ABAAABA. An aqueous sensor featuring a specific defective structure of quasi-periodic phononic crystals (PnCs) was created by placing a defect layer between two identical designs that followed similar Fibonacci sequence patterns. As a result, the S4 series was utilized to differentiate between the two sequences, with the Octonacci sequence pattern depicted in Figure 1b.

Now, a discussion is provided on how the S_n quasi-periodic PnC structures were created using the Thue–Morse sequence, as shown in Figure 1c. The Thue–Morse sequence is assumed in various ways; however, it can be easily shown that they are interchangeable [43]. To put it simply, the recursive relations are as follows:

$$S_n = S_{n-1}S_{n-1}^+ \text{ and } S_n^+ = S_{n-1}^+ S_{n-1} \text{ (for } n \geq 1) \tag{3}$$

Here, S_0 = A and S_0^+ = B, which are used to deduce the Thue–Morse sequence, and by utilizing the rules of addition A $\rightarrow$ AB and B $\rightarrow$ BA, this sequence can also be constructed in another method. Accordingly, the generations of the Thue–Morse sequence are S_0 = A, S_1 = AB, S_2 = ABBA, S_3 = ABBABAAB, and so on.

The last example illustrated here is a double-period sequence, which is classified as the newest form of aperiodic chains. It was initially established in studies on laser applications using nonlinear optical fibers as well as studies on dynamic systems [44]. The nth order of this sequence is given as follows:

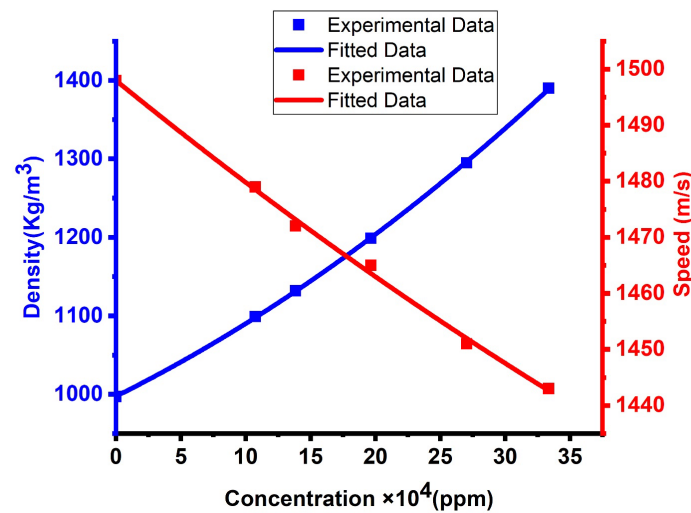$$S_n = S_{n-1}S_{n-1}^+ \text{ and } S_n^+ = S_{n-1} \, S_{n-1} \text{ (for } n \geq 1) \tag{4}$$

where S_0 = A and S_0^+ = B. This recursion relationship is slightly comparable to the Thue–Morse instance. It remains invariant whenever A $\rightarrow$ AB and B $\rightarrow$ AA are used. Thus, the generations of the double-period are S_0 = A, S_1 = AB, S_2 = ABAA, S_3 = ABAAABAB, etc.

2.2. Acoustic Properties of Pb(NO₃)₂

Many previous studies have investigated the effects of changing $Pb(NO_3)_2$ concentrations on its acoustic characteristics, including sound speed and mass density [45–47]. Thus, the main relationship between the solution's concentration and its acoustic properties was ascertained by analyzing the collected data. The findings indicated that the mass density of the solution increased linearly as the concentration of $Pb(NO_3)_2$ increased. This is supported by the fitting of the data to the polynomial equation (Equation (5)) [45,47], which is expressed as follows:

$$\rho \left(\frac{\text{Kg}}{\text{m}^3} \right) = \alpha + \beta \times C \, (\text{ppm}) + \gamma \times C^2 \left(\text{ppm}^2 \right) \tag{5}$$

Here, ρ denotes the mass density, C is the concentration, and α and β and γ denote the coefficients that result from this fitted relationship. Based on the calculations, the values of α, β, and γ were found to be 997.54799, 8.2023×10^{-4} and 1.05846×10^{-9}, respectively. Equation (5) depicts a consistent nonlinear relationship, as demonstrated in Figure 2.

Figure 2. Acoustic properties of Pb(NO$_3$)$_2$ solution versus its concentration.

This, in turn, indicates that the solution's concentration is linearly associated with density, confirming that the number of dissolved solute molecules grows, which consequently results in a greater mass per one-unit volume. The experimental data obtained regarding the sound speed of Pb(NO$_3$)$_2$ were evaluated and fitted to a polynomial fitting equation, which is illustrated in the following equation [45,47]:

$$v\left(\frac{\text{m}}{\text{sec}}\right) = \sigma + \epsilon \times C\,(\text{ppm}) + \delta \times C^2\left(\text{ppm}^2\right) \tag{6}$$

Here, v represents the Pb(NO$_3$)$_2$ speed of sound, C represents its concentration, and σ and ϵ and δ represent the generated coefficients by the given fitted relationship and were found to be 1498.00935, -1.88615×10^{-4}, and 6.81655×10^{-11}, respectively.

As shown in Figure 2, the sound velocity of Pb(NO$_3$)$_2$ increased as its concentration decreased, which is consistent with the polynomial relationship described by Equation (6). As displayed in Figure 2, the concentration of Pb(NO$_3$)$_2$ increased, while the sound velocity decreased, leading to a polynomial fitting that corresponds to Equation (6). A variable-path interferometer represents an experimental device, which was utilized to study ultrasonic velocity as an indicator of lead nitrate aqueous solution's concentration [48–50].

2.3. Theoretical Treatment

Over the last thirty years, the transfer matrix method (TMM) has been used as the most preferred and efficient approach to theoretically understand the acoustic wave interaction with the PnC structure. This study aimed to clarify the method used for assessing the proposed structure's transmission spectrum while interacting with acoustic waves [51,52]. The method used entailed subjecting a single 1D PnC unit cell to acoustic waves, (see Figure 1) and computing a generalized equation for the whole framework. Acoustic wave interaction could only occur through the provided *x*-axis, and every unit cell was composed of two layers of lead–epoxy with d$_1$ and d$_2$ layer thicknesses. Thus, the normal incidence ruling equation for the acoustic wave on the PnC structure is as follows:

$$\nabla^2\gamma = C_j^{-2}\ddot{\gamma}^2 \tag{7}$$

In the above, γ denotes the displacement potential; $C_i = \sqrt{\frac{\lambda+2\mu}{\rho}}$ indicates the acoustic wave velocity in every layer, i.e., layers of lead and epoxy; λ and μ denote Lamé coefficients;

and subscript $j = 1, 2$ denotes the PnC layer's number. Therefore, Equation (7) can be solved by using the following method:

$$\gamma = Xe^{i(\omega t - k_j x)} + Ye^{i(\omega t + k_j x)} \tag{8}$$

In the above instance, $i^2 = -1$; $k_j = \omega\sqrt{\frac{\rho_j}{Cxxx^j}}$ reflects the wave number in each single layer; ρ_j symbolizes mass density; ω represents the angular frequency; and $C_{xxx}{}^j$ is related to the given elastic strength, which is unchanged for a particular distinct layer, i.e., j. X and Y are two randomly independent coefficients. The stress components of the incident acoustic wave along the dimensionless displacement, the stress-related elements that comprise the incident acoustic wave, and the displacement are determined as follows [51–53]:

$$\overline{\sigma_x} = \lambda\left(\frac{\partial^2 \gamma}{\partial x^2}\right) + 2\mu\left(\frac{\partial^2 \gamma}{\partial x^2}\right) \tag{9}$$

$$\overline{v_x} = \frac{\partial \gamma}{\partial x} \tag{10}$$

The two-state vectors, which describe the entire propagation of acoustic waves at the layer's right/left sides, i.e., the jth layer in the kth unit, are given in the following manner:

$$V_{jL}^{(k)} = \left\{\overline{\sigma}_{xjL}^{(k)}, \overline{v}_{xjL}^{(k)}\right\} \tag{11}$$

$$V_{jR}^{(k)} = \left\{\overline{\sigma}_{xjR}^{(k)}, \overline{v}_{xjR}^{(k)}\right\} \tag{12}$$

The subscripts R and L might symbolize the layer's right side and its left side, that is, the jth layer. Thus, the layer's right/left state vectors as well as the jth layer in the stated kth unit cell are determined as follows:

$$V_{jR}^{(k)} = T_j' V_{jL}^{(k)} \tag{13}$$

where T_j' refers to a 2×2 transfer matrix; the components constitute the following:

$$T_j'(1,1) = T_j'(2,2) = \frac{\left[\exp(-iq_{Lj}x_j) + \exp(iq_{Lj}x_j)\right]}{2} \tag{14}$$

$$T_j'(1,2) = \frac{iq_{Lj}(\lambda + 2\mu) \cdot \left[\exp(iq_{Lj}x_j) - \exp(-iq_{Lj}x_j)\right]}{2} \tag{15}$$

$$T_j'(2,1) = \frac{i\left[\exp(iq_{Lj}x_j) - \exp(-iq_{Lj}x_j)\right]}{2q_{Lj}(\lambda + 2\mu)} \tag{16}$$

where $q_{Lj = \frac{\omega \, a}{Cl_j}}$ is a non-dimensional factor, and C_{Lj} is the speed of sound in each layer.

The correlation between the following consecutively state vectors in the specified kth, as well as $(k-1)$th unit cells, is determined with the following formula [53–55]:

$$V_{2R}^{(k)} = T_k V_{2R}^{(k-1)} \tag{17}$$

Thus, T_k is a predetermined transfer matrix that links two-unit cells; it is referred to as

$$T_k = T_2 T_1' \tag{18}$$

Following that, the transmission coefficient's incident acoustic waves using this PnC structure are described as follows:

$$\frac{U_e}{U_0} = \frac{2E_0(T_{11}T_{22} - T_{12}T_{21})}{E_0(T_{11} - E_e T_{21}) - (T_{12} - E_e T_{22})} \tag{19}$$

where E_0 and E_e refer to Young's moduli of the two semi-infinite solids at the left/right structures, whereas U_e and U_0 designate the incident and transmitted acoustic wave's amplitudes, with T_{ij} determining the elements of the transfer matrix's $T = T_n T_{n-1} \ldots T_k \ldots T_1$.
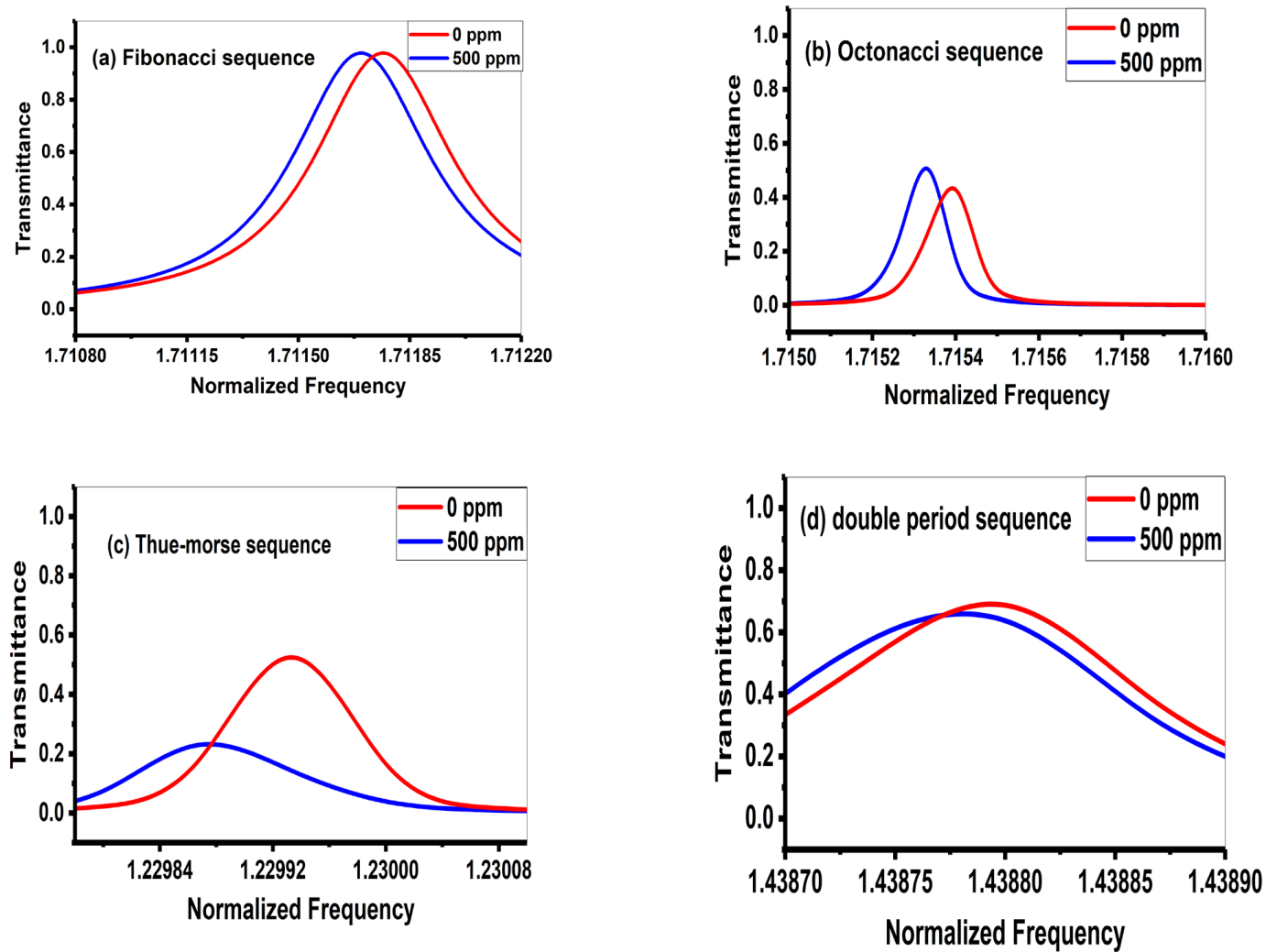
3. Results and Discussion

3.1. Comparison Between the Acoustic Spectra of the Different Quasi-Periodic Sequences for Pb(NO₃)₂ Solution

In this section, the transmission spectrum of different quasi-PnCs is studied and calculated by utilizing a filled defect layer with the $Pb(NO_3)_2$ aqueous solution in between. The relationship between the transmittance and the normalized frequency (f) is explored, which is given by the following formula [56]:

$$f = \frac{\omega \times a}{2\pi \, C} \tag{20}$$

where C is taken as the epoxy speed of sound, which is equivalent to $1160 \, \frac{m}{sec}$. We presume that the lead, epoxy, and $Pb(NO_3)_2$ defect layers' thicknesses are $d_1 = 0.5 \times 10^{-6}$ m and $d_2 = d_f = 0.1 \times 10^{-6}$ m, respectively. Figure 3 shows a comparative study of the transmittance spectra of the proposed designed sensor using the four different quasi-periodic patterns: Fibonacci, Octonacci, Thue–Morse, and double-period sequences. Figure 3a describes the 1D Fibonacci PnC structure's ($[(S_3) \, (Pb(NO_3)_2 \text{solution}) \, (S_3)]$) transmittance spectrum at two different concentrations of $Pb(NO_3)_2$. At a zero concentration of $Pb(NO_3)_2$ through the defect layer, the figure shows the presence of a defect mode at a normalized frequency of 1.71, which is equivalent to 3.3093 GHz. As the defect layer is filled with the $Pb(NO_3)_2$ of concentration = 5000 ppm, the defect mode shifts to a new normalized frequency = 1.71, which matches 3.30 GHz. Thus, changing the $Pb(NO_3)_2$ concentration led to several changes in the defect layer's acoustic properties (sound speed and density), as indicated in Figure 2, which, in turn, led to a position shift in the generated defect mode. Remarkably, this shift clarifies that the designed 1D Fibonacci PnC sensor provides a comparatively higher sensitivity of 232 Hz/ppm. Regarding the 1D Octonacci PnC design in Figure 3b, the transmittance spectrum exhibits a different response compared to that of the Fibonacci one. Moreover, the transmissivity of the introduced resonant mode starts to decrease. This response could be due to the change in the path length of the acoustic waves due to the change in the geometry of the designed sensor. Meanwhile, the resonant mode shifted from 3.315 GHz to 3.317 GHz due to the change in the $Pb(NO_3)_2$ concentration through the given defect layer (0–5000 ppm), correspondingly. Therefore, the designed sensor exhibited a sensitivity of 254.3 GHz/ppm. For the Thue–Morse and double-period sequences, as shown in Figure 3c,d, respectively, the defect modes received new positions. In addition, the full width of these modes provides relatively large values compared to those of the Fibonacci and Octonacci sequences. However, the designed 1D Thue–Morse PnC sensor exhibited a sensitivity of 232 Hz/ppm due to the shift in the frequency of the resonant mode between 2.377 GHz and 2.378 GHz. In contrast, the 1D double-period PnC design exhibited a comparatively higher sensitivity of 502.667 Hz/ppm because of the position shift in the given defect mode (2.7815 GHz–2.7819 GHz). Consequently, the design for the 1D PnC sensor in accordance with the double-period sequence represents the optimum choice for the detection of $Pb(NO_3)_2$ and many other liquids. This quasi-periodic sequence, therefore, exhibits a greater degree of autonomy and adaptability for the characteristics of the proposed building structure. Additionally, the quasi-periodic designs allow for the anticipation of the strong resonance modes, which disrupt the periodicity of the structure to create resonance, and it is more sensitive than other sequences [57,58]. Thus, this sequence was kept, and its performance analysis was calculated.
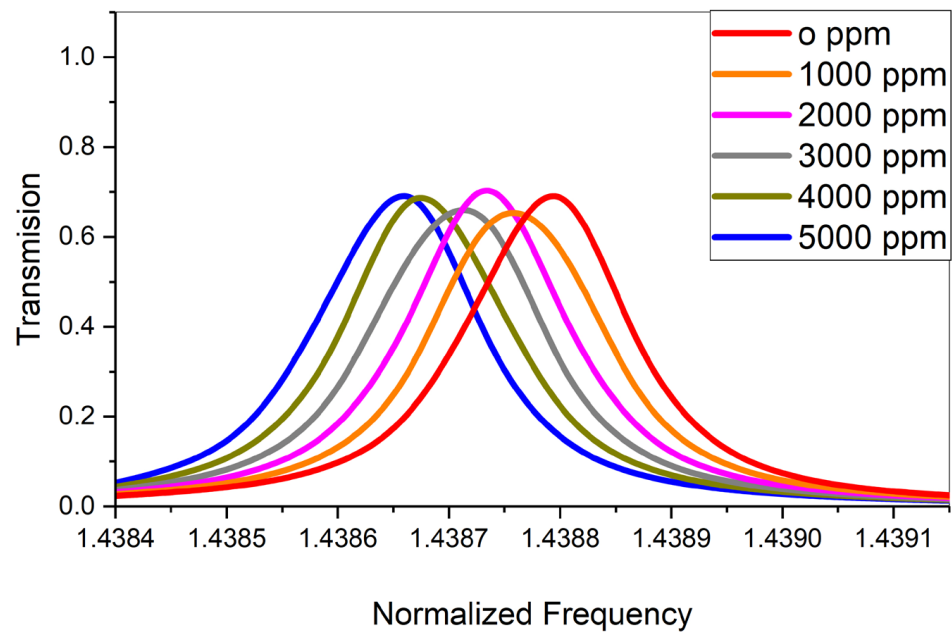
Figure 3. (**a**) S_3 Fibonacci sequence [(S_3) $(Pb(NO_3)_2$ solution$)$ $(S_3$)]; (**b**) Octonacci sequence [(S_4) $(Pb(NO_3)_2$ solution$)$ $(S_4$)]; (**c**) Thue–Morse sequence [(S_3) $(Pb(NO_3)_2$ solution$)$ $(S_3$)]; (**d**) double-period sequence [(S_3) $(Pb(NO_3)_2$ solution$)$ $(S_3$)].

3.2. Multi-Concentration Effects of $Pb(NO_3)_2$ Aqueous Solution on the Double-Period S_3 Quasi-Periodic Crystal

This section provides a detailed account of how the increasing concentration of $Pb(NO_3)_2$ impacts the transmittance of the optimized 1D phononic crystal (PnC) sensor. Figure 4 illustrates the resonance mode shift resulting from incremental concentrations of the proposed analyte, ranging from 0 to 5000 ppm, including key concentrations like 1000 ppm, 2000 ppm, 3000 ppm, and 4000 ppm. The figure demonstrates a downward shift in the resonant mode position toward lower normalized frequency values. Specifically, the defect mode shifts from 2.780 GHz to 2.782 GHz. The analysis reveals that the higher analyte concentrations induce notable changes in the acoustic properties of the defect layer. Notably, Figure 2 showcases a substantial decrease in density with rising analyte concentrations, while the sound speed experiences increments. The sensor's sensitivity increased from 5255.18 Hz/ppm to 6689.33 Hz/ppm as the analyte concentration increased from 0 ppm to 5000 ppm.

Figure 4. Effect of multiple concentrations on the transmittance properties of S_3 double-period quasi-periodic PnC structure.

3.3. Sensor Performance Analysis

Finally, this subsection discusses the performance of the 1D double-period PnC sensor considered in this study. The S_3 double-period quasi-periodic structure showed great sensitivity, which can be the most effective PbNO$_3$ sensor framework based on previous studies. Meanwhile, some key parameters closely related to establishing how effectively the suggested sensor works were utilized to analyze the sensing tool's effectiveness in this study. These factors were QF for the quality factor, FOM for the figure of merit, and S for sensitivity. The defect mode properties can considerably influence these parameters and the sensor's performance. The position shift in the given resonant mode in response to the concentration variations describes the sensor's sensitivity as follows [59,60]:

$$S = \Delta f / \Delta x \tag{21}$$

Therefore, the value of the variable Δx signifies an alteration in the concentration of the utilized analyte (PbNO$_3$), whereas Δf indicates the resonant peak or the designated frequency at varying concentrations. The quality factor (QF), a computed performance measurement, is contingent upon the exact position of the resonance peak [59,60] and is determined as follows:

$$QF = f_r / f_{HBW} \tag{22}$$

where f_{HBW} symbolizes the frequency at half-bandwidth of the resonant peak, and f_r corresponds to the frequency at which it resonates. The intense resonant peaks that demonstrate the high-quality factor therefore enhanced the resolution of that resonant frequency. The figure of merit (*FOM*) parameter shows the sensor's capability of monitoring any resonant frequency changes with high precision and efficiency [61,62] and is determined as follows:

$$FOM = S / f_{HBW} \tag{23}$$

Due to the inverse relationship between the *FOM* and the frequency at the resonant peak's half-bandwidth, the decreased frequency at the resonant peak's half-bandwidth resulted in increased *FOM*. Then, the smallest possible level of concentration or quantity of a material consistently identified through a specific analytic technique is referred to as

the limit of detection (*LOD*). The sensor's effectiveness is enhanced with a reduced limit of detection, enabling it to identify extremely low levels [63–65].

$$LOD = 0.05/FOM \tag{24}$$

The damping rate, i.e., the most significant indication of efficiency, measures how sound waves diminish within the planned PnCs, adhering to a specific structural disruption, in addition to regulating the extent of the sharpness of the resonance-transmitted peaks [66–69].

$$\zeta = 0.5/QF \tag{25}$$

By studying the *FOM*, *QF*, and the damping rate (ζ), the results, in general, show that the S_3 double-period quasi-periodic structure symbolizes an effective sensor framework for detecting the solution of lead nitrate($PbNO_3$), displaying greater performance and sensitivity. The fabrication of highly sensitive and precise sensing devices may be considerably influenced by these findings.

Analysis of the Performance of the $PbNO_3$ Sensor

Figure 5a exhibits the effect of the concentration variation on the $PbNO_3$ solution liquid sensor's resonance peaks, affecting its sensitivity. As is observed, the resonant modes change linearly relative to higher frequencies as the concentration of the solution of $PbNO_3$ is higher, which in turn enhances the sensor's sensitivity. As a result, as shown in Figure 5a, the recommended PnC sensor design can provide excellent sensitivity and performance rates at varying concentrations ranging from 0 ppm to 5000 ppm. Whenever the concentrations fluctuated between 0 ppm to 5000 ppm, the design that had been implemented yielded a significantly greater sensitivity (6689.33 Hz/ppm) for the selected quasi-periodic structure. However, the results revealed a gradual decline while sensitivity increased to 5255.18 Hz/ppm for the given quasi-periodic structures at 5000 ppm. Consequently, when contrasted with earlier sensors or designs, the sensitivity of the suggested design is promising.
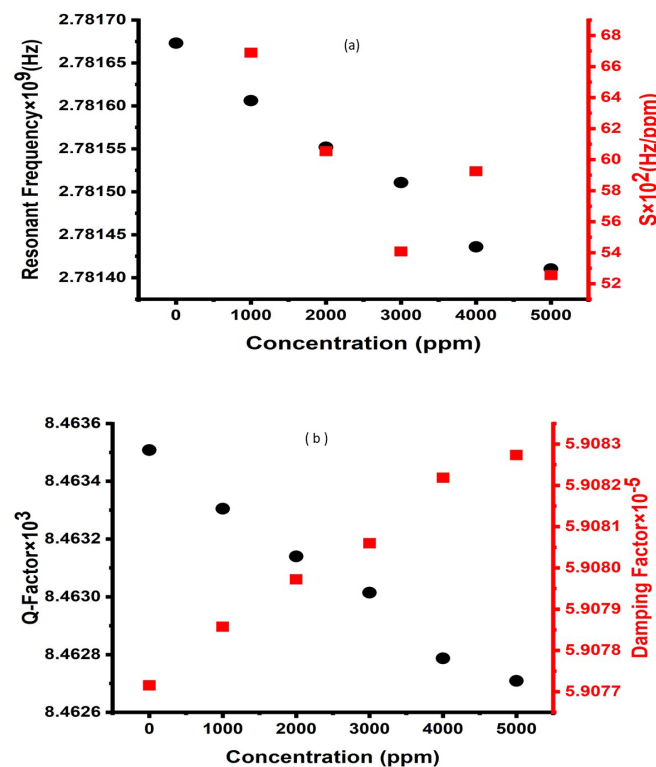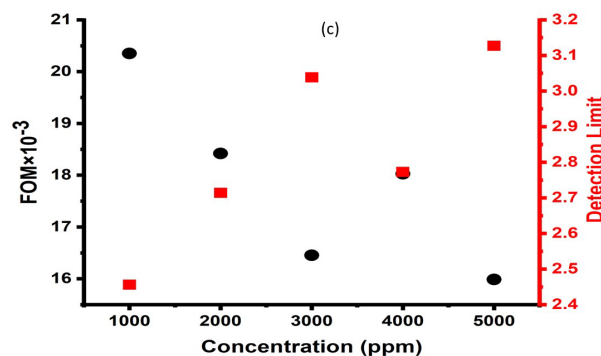

Figure 5. *Cont.*

Figure 5. The performance parameters of the S_3 double-period quasi-periodic PnC structure are (**a**) the sensitivity and resonance peaks, (**b**) the damping rate and quality factor, and (**c**) the detection limit and figure of merit.

Figure 5b shows how the QF of the proposed design is affected by the rate of damping of the sound waves. Therefore, it demonstrates that when the *PbNo₃* solution concentration was 0 ppm, and the damping rate was at its lowest level of 5.9×10^{-5}, the greatest *QF* value of 8463.5 was obtained. On the other hand, the highest rate of damping of 5.9×10^{-5}, and its smallest *QF* value of 8462.7 was found at 5000 ppm of $PbNO_3$ concentration. The *QF*, whose value varied from 8463.508529 to 8462.7, was extremely high considering the difference in the concentrations of the analyte. Therefore, all the resonant peaks demonstrated a sharp appearance, incorporating the resolution of frequencies of the newly developed sensing tool. The inverse correlation between the damping rate and the quality factor is demonstrated. Lower damping rates led to a lower full width at half-maximum and higher values of *QF*. Low damping rates, however, can be a disadvantage since they suggest that the structure is not capable of absorbing the incoming sound waves as it should be. The recommended PnC sensor construction differs in several ways in comparison to the 1D PnC generations, which have been explored in previous investigations [70,71]. The sensor investigated in [70] performed satisfactorily regardless of the concentrations of NaI–water. In this instance, the sensor's sensitivity for a concentration that ranged from 6% to 7% was 1714 Hz, with a quality factor of 1401 and a *FOM* of 28. The sensor investigated in [71] exhibited impressive sensitivity, reaching a value of 1275 Hz. As a result, the *FOM* could increase to 910. The sensor was developed into a four-channel demultiplexer that was adjustable and capable of separating nearby frequencies, each of which is related to the concentration of $PbNO_3$ solution. Based on the findings, it may be claimed that the presented PnC sensor design is a very attractive option, which can be used for extremely sensitive and reliable sensing applications. This can be attributed to its sharp resonant peaks and high *QF*, as well as the *FOM* and the LOD of the recommended PnC $PbNO_3$ solution liquid sensor. The relationship between the $PbNO_3$ solution concentrations and the estimated sensor's limit for detection can be observed in Figure 5c. The results demonstrated that the detection limit dropped from 2.456647399 to 3.127069384 as the $PbNO_3$ solution concentration increased from 0 to 5000 ppm. When measured against different liquid sensor designs of comparable shapes and dimensions, the obtained values were deemed to be suitable. Additionally, the FOM of the sensor was investigated, and the findings revealed a decline in FOM with a rise in the $PbNO_3$ concentration. The FOM values varied when the analyte concentration increased from 0 ppm to 5000 ppm, with values ranging from 0.01 to 0.02.

To summarize, Table 2 provides a comparison between the constructed sensors in this study with similar sensing tools. This study is a comprehensive survey of 1D PnC sensors and provides different PnC structures based on quasi-period sequences. As illustrated in Table 2, the proposed sensor in this study has a very high sensitivity in comparison with similar sensors, making it an efficient sensing tool for the $PbNO_3$ aqueous solution and other fluidic solutions.

Table 2. Comparison between the results obtained in this study and previous sensors.

Type of Sensor	Sensing Material	Figure of Merit	Sensitivity	Reference
Three-dimensional sensor for the phononic crystal fluidic sensing tool.	NaCl	–	(Experimentally) 1.4×10^3 Hz	[69]
Two-dimensional biosensor for the detection of NaI based on the phononic crystal.	NaI–water	28	1833 Hz	[70]
A liquid sensor is used as a DE multiplexing wave in a two-dimensional biosensor based on the phononic crystal.	Vinegar	910	1275 Hz	[71]
One-dimensional glycine sensor based on the phononic crystal.	Glycine	4.2	969, 973 Hz	[62]
This research	Lead nitrate $Pb(NO_3)_2$	0.020352941	5255.19:6689.33 Hz/ppm	

3.4. Comparison with Previous Sensors

Finally, in this section, we compare the most important performance parameters that determine the sensitivity and figure of merit of the proposed sensor. A comparison of the parameters obtained in this study with those of previous studies is presented in Table 2. Abdulkarem et al. thoroughly explored the utilization of periodic and quasi-periodic one-dimensional (1D)-layered phononic crystals (PnCs) as highly sensitive biosensors for detecting and monitoring sodium iodide (NaI) solution. Our research exceeds this study in both the quality factor and detection limit values. Specifically, it revealed a quality factor of 8463.5 with a lower damping rate, underscoring the superior performance of the proposed sensor compared to the one presented in this study, which has a quality factor of 6947 and a higher damping rate [39].

Abdulkarem et al. used two PnC designs (periodic and quasi-periodic) to detect CO_2 pollution in the surrounding air across a wide range of concentrations (0–100%). Our research surpasses this study in the quality factor, demonstrating a superior quality factor of 8463.5. This highlights the significance of the proposed sensor compared to the sensor in this study, which has a lower quality factor of 280 [68].

3.5. Losses and Damping of the Proposed Sensor

Firstly, we will discuss "the reason for transmission coefficients below 1 at resonance". Physically, as is well known, resonance peaks and band gaps result mainly from Bragg's law; this is the governing rule in all band gap materials, as constructive interference results in the formation of stop bands, and destructive interference results in the formation of passbands. Some resonant peaks or dips may appear due to the high confinement of waves through specific cavities or defects. These peaks are sometimes called slow modes or modes with low group velocity; see our previous paper in [71]. These modes physically result from the coupling between the high resonance in liquid (water in this study) and evanescent modes in solid materials (Pb and epoxy in this study). Therefore, these peaks are confined to specific frequency and transmission values. This transmission intensity or position is determined based on the properties of the analyte material and surrounding materials. In this regard, acoustic mismatch and acoustic impedance ($z = \rho v$) between the building materials represent a key factor in Bragg's law and band formation as each analyte's building blocks involving peaks with specific intensity and position are based on acoustic impedance; indeed, this peak formation is a common result that may even indicate the presence of losses and attenuation. Surely, losses may affect the position and more especially the peak intensity. This effect appears clearly in low-dimension structures (100 nm or smaller) [72]. Based on this view, in our paper, as seen in Figure 4, all peaks had high intensity (higher than 70%), and their intensities did not differ greatly with changes in heavy metal concentrations (as the variation is in the ppm scale). Finally, in some designs, when stacking materials with a higher mismatch (like Pb or silicone and rubber) and other

liquids, the resonant peaks are confined to values with greater intensity than those reported in this design for filtering purposes; see reference [13].

Generally, for a compressible Newtonian fluid, the effect of viscosity on wave propagation through a liquid medium is described based on Navier–Stokes equations, which is given as follows [73,74]:

$$i\omega\rho_{liq}v = -\nabla p + \nabla.\left(\mu\left[\nabla v + (\nabla v)^T\right] - \left[\frac{2}{3}\mu - \mu_B\right][\nabla.v]\overleftrightarrow{I}\right) \text{ With } v = \frac{j}{\omega\rho_{liq}}\nabla p \quad (26)$$

where v is the sound speed, and μ and μ_B are the shear and bulk viscosity, respectively. P is the acoustic pressure. In the above equations, the thermal effects are ignored as well. In the current design, all solutions in the defect layer were only water, and there were no changes in concentration at high levels (%) or type (like honey, milk, or highly viscous liquid). Therefore, if we assume that the viscosity affects the intensity of the resonance peak, and hence this intensity decreases, in all cases, the peak intensity does not decrease to a dramatic value that may change or affect the idea of our paper, as confirmed in reference [72]. In addition to that, in all heavy metal concentrations, the peak intensity was the same as no liquid or another type was used in the defect layer, and surely our case here is a special case for heavy metals in ppm levels specifically. Lastly, concerning changes in the sound speed with frequency, many previous studies have proved that elastic parameters are stable with frequency at higher frequencies [73,74]. In this design, we proposed the application of the GHz regime.

4. Conclusions

The objective of this research was to evaluate the effectiveness of fluidic and aqueous solutions. Specifically, the lead nitrate $Pb(NO_3)_2$ aqueous solution, classified as a fluidic material, was examined across concentrations ranging from 0 ppm to 5000 ppm. The core of the detection method relies on tracking the shift in the position of transmitted resonant peaks within the phononic band gaps. The double-period, Fibonacci, Octonacci, and Thue–Morse sequences were investigated to obtain the optimal performance of the sensor. Thus, the findings demonstrated that the double-period PnC, particularly the S3 sequence, represents the most sensitive quasi-periodic sequence. According to the results, the S3 quasi-periodic PnC structure showed a considerable sensitivity of approximately 502.66 Hz/ppm, which is the highest obtained sensitivity for heavy metal solutions and biomaterials in a PnC framework. The constructed sensor demonstrated a high-quality factor (QF) of 8463.508, a figure of merit (FOM) of 2.45, and a damping rate at the lowest feasible level of 5.9×10^{-5}. The transfer matrix technique (TMM) was used to theoretically predict the transmission spectrum of the proposed sequences. The results demonstrate a simple biosensor design for detecting different liquids and biofluids. The built-in simplicity, affordability, and the use of easily obtained components are the primary advantages of the proposed PnC sensor in this study.

Author Contributions: Project administration, M.T., S.B., A.M., A.H., M.R.A. and H.A.E.; supervision, M.T., S.B., A.M., A.H. and H.A.E.; software, A.G.S., A.M. and H.A.E.; visualization, A.M. and A.G.S.; writing—review and editing, A.G.S., A.H., A.M. and H.A.E.; writing—original draft preparation, A.G.S., A.H. and A.M.; methodology, A.M. and A.G.S. All authors have read and agreed to the published version of the manuscript.

Data Availability Statement: The datasets used and/or analyzed during the current study are available from the corresponding author upon reasonable request.

Conflicts of Interest: The authors declare no conflicts of interest.

References

1. Lee, G.; Lee, S.-J.; Rho, J.; Kim, M. Acoustic and mechanical metamaterials for energy harvesting and self-powered sensing applications. *Mater. Today Energy* **2023**, *37*, 101387. [CrossRef]
2. Li, W.; Meng, F.; Chen, Y.; Li, Y.F.; Huang, X. Topology optimization of photonic and phononic crystals and metamaterials: A review. *Adv. Theory Simul.* **2019**, *2*, 1900017. [CrossRef]
3. Oudich, M.; Gerard, N.J.; Deng, Y.; Jing, Y. Tailoring structure-borne sound through bandgap engineering in phononic crystals and metamaterials: A comprehensive review. *Adv. Funct. Mater.* **2023**, *33*, 2206309. [CrossRef]
4. Oudich, M.; Gerard, N.J.; Deng, Y.; Jing, Y. Bandgap engineering in phononic crystals and elastic metamaterials. *arXiv* **2022**, arXiv:2207.05234.
5. Su, Y.; Ma, C.; Chen, J.; Wu, H.; Luo, W.; Peng, Y.; Luo, Z.; Li, L.; Tan, Y.; Omisore, O.M.; et al. Printable, highly sensitive flexible temperature sensors for human body temperature monitoring: A review. *Nanoscale Res. Lett.* **2020**, *15*, 200. [CrossRef]
6. Fedder, G.K.; Howe, R.T.; Liu, T.-J.K.; Quevy, E.P. Technologies for cofabricating MEMS and electronics. *Proc. IEEE* **2008**, *96*, 306–322. [CrossRef]
7. Lucklum, R.; Mukhin, N.; Rouhani, B.D.; Pennec, Y. Phononic crystal sensors: A new class of resonant sensors—Chances and challenges for the determination of liquid properties. *Front. Mech. Eng.* **2021**, *7*, 705194. [CrossRef]
8. Westafer, R.S. *Investigation of Phononic Crystals for Dispersive Surface Acoustic Wave Ozone Sensors*; Georgia Institute of Technology: Atlanta, Georgia, 2011.
9. Mehaney, A.; Nagaty, A.; Aly, A.H. Glucose and hydrogen peroxide concentration measurement using 1D defective phononic crystal sensor. *Plasmonics* **2021**, *16*, 1755–1763. [CrossRef]
10. Lucklum, R.; Ke, M.; Zubtsov, M. Two-dimensional phononic crystal sensor based on a cavity mode. *Sens. Actuators B Chem.* **2012**, *171*, 271–277. [CrossRef]
11. Biçer, A.; Cicek, A. Liquid concentration sensing via weakly coupled point defects in a phononic crystal. *J. Mol. Liq.* **2024**, *409*, 125487. [CrossRef]
12. Zaki, S.E.; Mehaney, A.; Hassanein, H.M.; Aly, A.H. Fano resonance based defected 1D phononic crystal for highly sensitive gas sensing applications. *Sci. Rep.* **2020**, *10*, 17979. [CrossRef] [PubMed]
13. Imanian, H.; Noori, M.; Abbasiyan, A. Highly efficient gas sensor based on quasi-periodic phononic crystals. *Sens. Actuators B Chem.* **2021**, *345*, 130418. [CrossRef]
14. Basyooni, M.A.; Zaki, S.E.; Ertugrul, S.; Yilmaz, M.; Eker, Y.R. Fast response of CO_2 room temperature gas sensor based on Mixed-Valence Phases in Molybdenum and Tungsten Oxide nanostructured thin films. *Ceram. Int.* **2020**, *46*, 9839–9853. [CrossRef]
15. Vardhan, K.H.; Kumar, P.S.; Panda, R.C. A review on heavy metal pollution, toxicity and remedial measures: Current trends and future perspectives. *J. Mol. Liq.* **2019**, *290*, 111197. [CrossRef]
16. Gautam, P.K.; Gautam, R.K.; Banerjee, S.; Chattopadhyaya, M.; Pandey, J. Heavy metals in the environment: Fate, transport, toxicity and remediation technologies. *Nova. Sci. Publ.* **2016**, *60*, 101–130.
17. Pandey, G.; Madhuri, S. Heavy metals causing toxicity in animals and fishes. *Res. J. Anim. Vet. Fish. Sci.* **2014**, *2*, 17–23.
18. Siegel, F.R. *Environmental Geochemistry of Potentially Toxic Metals*; Springer: Berlin/Heidelberg, Germany, 2002; Volume 32.
19. Rehman, K.; Fatima, F.; Waheed, I.; Akash, M.S.H. Prevalence of exposure of heavy metals and their impact on health consequences. *J. Cell. Biochem.* **2018**, *119*, 157–184. [CrossRef]
20. Järup, L. Hazards of heavy metal contamination. *Br. Med. Bull.* **2003**, *68*, 167–182. [CrossRef]
21. Masindi, V.; Muedi, K.L. Environmental contamination by heavy metals. *Heavy Met.* **2018**, *10*, 115–132.
22. Mishra, S.; Bharagava, R.N.; More, N.; Yadav, A.; Zainith, S.; Mani, S.; Chowdhary, P. Heavy metal contamination: An alarming threat to environment and human health. In *Environmental Biotechnology: For Sustainable Future*; Springer: Berlin/Heidelberg, Germany, 2019; pp. 103–125.
23. Duruibe, J.; Ogwuegbu, M.O.C.; Egwurugwu, J. Heavy metal pollution and human biotoxic effects. *Int. J. Phys. Sci.* **2007**, *2*, 112–118.
24. Okereafor, U.; Makhatha, M.; Mekuto, L.; Uche-Okereafor, N.; Sebola, T.; Mavumengwana, V. Toxic metal implications on agricultural soils, plants, animals, aquatic life and human health. *Int. J. Environ. Res. Public Health* **2020**, *17*, 2204. [CrossRef] [PubMed]
25. Rahman, Z.; Singh, V.P. The relative impact of toxic heavy metals (THMs)(arsenic (As), cadmium (Cd), chromium (Cr)(VI), mercury (Hg), and lead (Pb)) on the total environment: An overview. *Environ. Monit. Assess.* **2019**, *191*, 419. [CrossRef] [PubMed]
26. Mahurpawar, M. Effects of heavy metals on human health. *Int. J. Res. Granthaalayah* **2015**, *530*, 1–7. [CrossRef]
27. World Health Organization. *Lead: Environmental Aspects*; World Health Organization: Geneva, Switzerland, 1989.
28. Casas, J.S.; Sordo, J. *Lead: Chemistry, Analytical Aspects, Environmental Impact And Health Effects*; Elsevier: Amsterdam, The Netherlands, 2011.
29. Lucklum, R.; Zubtsov, M.; Ke, M. Liquid sensor utilizing a regular phononic crystal with normal incidence of sound. *IEEE Trans. Ultrason. Ferroelectr. Freq. Control* **2012**, *59*, 463–471. [CrossRef] [PubMed]
30. Pierro, V.; Galdi, V.; Castaldi, G.; Pinto, I.M.; Felsen, L.B. Radiation properties of planar antenna arrays based on certain categories of aperiodic tilings. *IEEE Trans. Antennas Propag.* **2005**, *53*, 635–644. [CrossRef]
31. Crescitelli, A.; Ricciardi, A.; Consales, M.; Esposito, E.; Granata, C.; Galdi, V.; Cutolo, A.; Cusano, A. Nanostructured metallo-dielectric quasi-crystals: Towards photonic-plasmonic resonance engineering. *Adv. Funct. Mater.* **2012**, *22*, 4389–4398. [CrossRef]

32. Walter, S.; Deloudi, S.; Steurer, W.; Deloudi, S. Tilings and Coverings. In *Crystallography of Quasicrystals: Concepts, Methods and Structures*; Springer: Berlin/Heidelberg, Germany, 2009; pp. 7–47.

33. Baseri, A.; Keshavarz, A. Designing a double-negative metamaterial photonic crystal using the Thue–Morse sequence. *J. Comput. Electron.* **2022**, *21*, 270–279. [CrossRef]

34. Manzanares-Martínez, B.; Sánchez-Dehesa, J.; Håkansson, A.; Cervera, F.; Ramos-Mendieta, F. Experimental evidence of omnidirectional elastic bandgap in finite one-dimensional phononic systems. *Appl. Phys. Lett.* **2004**, *85*, 154–156. [CrossRef]

35. Lee, J.H.; Koh, C.Y.; Singer, J.P.; Jeon, S.J.; Maldovan, M.; Stein, O.; Thomas, E.L. 25th anniversary article: Ordered polymer structures for the engineering of photons and phonons. *Adv. Mater.* **2014**, *26*, 532–569. [CrossRef]

36. Zhang, Z.; Han, X. A new hybrid phononic crystal in low frequencies. *Phys. Lett. A* **2016**, *380*, 3766–3772. [CrossRef]

37. Assouar, M.B.; Sun, J.-H.; Lin, F.-S.; Hsu, J.-C. Hybrid phononic crystal plates for lowering and widening acoustic band gaps. *Ultrasonics* **2014**, *54*, 2159–2164. [CrossRef] [PubMed]

38. Almawgani, A.H.; Fathy, H.M.; Ali, G.A.; Elsayed, H.A.; Mehaney, A. One-dimensional phononic crystals: A simplified platform for effective detection of heavy metals in water with high sensitivity. *Micromachines* **2023**, *14*, 204. [CrossRef] [PubMed]

39. Almawgani, A.H.; Fathy, H.M.; Elsayed, H.A.; Ali, G.A.; Irfan, M.; Mehaney, A. Periodic and quasi-periodic one-dimensional phononic crystal biosensor: A comprehensive study for optimum sensor design. *RSC Adv.* **2023**, *13*, 11967–11981. [CrossRef] [PubMed]

40. Morfonios, C.; Schmelcher, P.; Kalozoumis, P.; Diakonos, F. Local symmetry dynamics in one-dimensional aperiodic lattices: A numerical study. *Nonlinear Dyn.* **2014**, *78*, 71–91. [CrossRef]

41. Moustaj, A.; Röntgen, M.; Morfonios, C.V.; Schmelcher, P.; Smith, C.M. Spectral properties of two coupled Fibonacci chains. *New J. Phys.* **2023**, *25*, 093019. [CrossRef]

42. Biasco, S.; Ciavatti, A.; Li, L.; Davies, A.G.; Linfield, E.H.; Beere, H.; Ritchie, D.; Vitiello, M.S. Highly efficient surface-emitting semiconductor lasers exploiting quasi-crystalline distributed feedback photonic patterns. *Light Sci. Appl.* **2020**, *9*, 54. [CrossRef]

43. Prokopenko, M.; Boschetti, F.; Ryan, A.J. An information-theoretic primer on complexity, self-organization, and emergence. *Complexity* **2009**, *15*, 11–28. [CrossRef]

44. Albuquerque, E.L.; Cottam, M.G. Theory of elementary excitations in quasiperiodic structures. *Phys. Rep.* **2003**, *376*, 225–337. [CrossRef]

45. Subrahmanyam, S.; Bhimasenachar, J. Ultrasonic Studies in Melts and Solutions. *J. Acoust. Soc. Am.* **1960**, *32*, 703–705. [CrossRef]

46. Candel, S.M. A review of numerical methods in acoustic wave propagation. In *Recent Advances in Aeroacoustics: Proceedings of an International Symposium Held at Stanford University, Stanford, CA, USA, 22–26 August 1983*; Springer: New York, NY, USA, 1986; pp. 339–410.

47. Yazdani-Darki, S.; Eslami-Kalantari, M.; Zare, H. Study of double-using ultrasonic effects on the structure of PbO nanorods fabricated by the sonochemical method. *Ultrason. Sonochemistry* **2021**, *79*, 105797. [CrossRef]

48. Voleišienė, B.; Voleišis, A. Ultrasound velocity measurements in liquid media. *Ultragarsas Ultrasound* **2008**, *63*, 7–19.

49. Nanda, A.; Tiadi, A.; Mallik, S.; Giri, R.; Nath, G. Ultrasonic characterization of silver nano fluid. In *IOP Conference Series: Materials Science and Engineering*; IOP Publishing Ltd.: Bristol, UK, 2018; p. 012064.

50. Dhal, K.; Singh, S.; Talukdar, M. Ultrasonic and Conductometric Studies on l-Aspartic Acid and l-Glutamic Acid in Aqueous Solutions of Sodium Acetate. *J. Solut. Chem.* **2023**, *52*, 1415–1445. [CrossRef]

51. Chen, A.-L.; Wang, Y.-S. Study on band gaps of elastic waves propagating in one-dimensional disordered phononic crystals. *Phys. B Condens. Matter* **2007**, *392*, 369–378. [CrossRef]

52. Wang, Y.-Z.; Li, F.-M.; Kishimoto, K.; Wang, Y.-S.; Huang, W.-H. Wave localization in randomly disordered layered three-component phononic crystals with thermal effects. *Arch. Appl. Mech.* **2010**, *80*, 629–640. [CrossRef]

53. Babiker, M.; Tilley, D.; Albuquerque, E.; Da Silva, C.G. Acoustic Green function for superlattices. *J. Phys. C Solid State Phys.* **1985**, *18*, 1269. [CrossRef]

54. Subrahmanyam, S. Ultrasonic behaviour of aqueous solutions of cadmium halides. *Trans. Faraday Soc.* **1960**, *56*, 971–974. [CrossRef]

55. Subrahmanyam, S. Ultrasonic velocities in aqueous solutions of cadmium iodide and mercuric chloride. *Nature* **1960**, *185*, 371. [CrossRef]

56. Burtis, W.; Helliwell, R. Magnetospheric chorus: Occurrence patterns and normalized frequency. *Planet. Space Sci.* **1976**, *24*, 1007–1024. [CrossRef]

57. Sun, C.; Li, J.; Jin, F.-F. A delayed oscillator model for the quasi-periodic multidecadal variability of the NAO. *Clim. Dyn.* **2015**, *45*, 2083–2099. [CrossRef]

58. Eccles, R.G. The quasifirm in the construction industry. *J. Econ. Behav. Organ.* **1981**, *2*, 335–357. [CrossRef]

59. Lucklum, R.; Zubtsov, M.; Arango, S.V. Cavity resonance biomedical sensor. In Proceedings of the ASME International Mechanical Engineering Congress and Exposition, Montreal, QC, Canada, 14–20 November 2014; p. V013T16A020.

60. Chen, Y.; Dong, J.; Liu, T.; Zhu, Q.; Chen, W. Refractive index sensing performance analysis of photonic crystal containing graphene based on optical Tamm state. *Mod. Phys. Lett. B* **2016**, *30*, 1650030. [CrossRef]

61. Hu, J.; Sun, X.; Agarwal, A.; Kimerling, L.C. Design guidelines for optical resonator biochemical sensors. *JOSA B* **2009**, *26*, 1032–1041. [CrossRef]

62. Khateib, F.; Mehaney, A.; Aly, A.H. Glycine sensor based on 1D defective phononic crystal structure. *Opt. Quantum Electron.* **2002**, *52*, 489. [CrossRef]

63. Lucklum, R.; Mukhin, N. Enhanced sensitivity of resonant liquid sensors by phononic crystals. *J. Appl. Phys.* **2021**, *130*, 024508. [CrossRef]

64. Villa-Arango, S.; Betancur, D.; Torres, R.; Kyriacou, P. Use of transient time response as a measure to characterize phononic crystal sensors. *Sensors* **2018**, *18*, 3618. [CrossRef]

65. Currie, L.A. Limits for qualitative detection and quantitative determination. Application to radiochemistry. *Anal. Chem.* **1968**, *40*, 586–593. [CrossRef]

66. Mukhin, N.; Oseev, A.; Kutia, M.; Borodacheva, E.; Korolev, P. Determination of ethanol content in fuels with phononic crystal sensor. *J. Russ. Univ. Radioelectron* **2019**, *22*, 107–115. [CrossRef]

67. Ke, M.; Zubtsov, M.; Lucklum, R. Sub-wavelength phononic crystal liquid sensor. *J. Appl. Phys.* **2011**, *110*, 026101. [CrossRef]

68. Almawgani, A.H.; Fathy, H.M.; Elsayed, H.A.; Ali, Y.A.A.; Mehaney, A. A promising ultra-sensitive CO_2 sensor at varying concentrations and temperatures based on Fano resonance phenomenon in different 1D phononic crystal designs. *Sci. Rep.* **2023**, *13*, 15028. [CrossRef]

69. Lucklum, F. Phononic-fluidic cavity sensors for high-resolution measurement of concentration and speed of sound in liquid solutions and mixtures. *Meas. Sci. Technol.* **2021**, *32*, 085108. [CrossRef]

70. Gharibi, H.; Mehaney, A.; Bahrami, A. High performance design for detecting NaI–water concentrations using a two-dimensional phononic crystal biosensor. *J. Phys. D Appl. Phys.* **2020**, *54*, 015304. [CrossRef]

71. Moradi, P.; Gharibi, H.; Fard, A.M.; Mehaney, A. Four-channel ultrasonic demultiplexer based on two-dimensional phononic crystal towards high efficient liquid sensor. *Phys. Scr.* **2021**, *96*, 125713. [CrossRef]

72. Saviot, L.; Netting, C.H.; Murray, D.B. Damping by Bulk and Shear Viscosity of Confined Acoustic Phonons for Nanostructures in Aqueous Solution. *J. Phys. Chem. B* **2007**, *111*, 7457–7461. [CrossRef] [PubMed]

73. Zhao, Y.P.; Wei, P.J. The band gap of 1D viscoelastic phononic crystal. *Comput. Mater. Sci.* **2009**, *46*, 603–606. [CrossRef]

74. Guo, F.; Guoy, H.; Sunz, P.; Yuanx, T.; Wang, Y. Study on band gap properties of two-dimensional phononic crystals based on generalized viscoelastic modeling. *Mod. Phys. Lett. B* **2019**, *33*, 1950403. [CrossRef]